Lattice Boltzmann method on unstructured grids: Further developments

S. Ubertini,[1] G. Bella,[1] and S. Succi[2]
[1]*Dipartimento di Ingegneria Meccanica, Universita' di Roma, Tor Vergata, Viale del Politecnico, 1, 00133, Roma, Italy*
[2]*Istituto Applicazioni Calcolo, CNR, Viale del Policlinico 137, 00161, Roma, Italy*
(Received 3 December 2002; published 11 July 2003)

We discuss further developments of the finite-volume lattice Boltzmann formulation on unstructured grids. It is shown that the method tolerates significant grid distortions without showing any appreciable numerical viscosity effects at second order in the mesh size. A theoretical argument of plausibility for such a property is presented. In addition, a set of boundary conditions which permit to handle flows with open boundaries is also introduced and numerically demonstrated for the case of channel flows and driven cavity flows.

DOI: 10.1103/PhysRevE.68.016701 PACS number(s): 47.11.+j, 05.20.Dd, 47.10.+g

INTRODUCTION

Recent advances in lattice Boltzmann research have lead to substantial enhancements of the capabilities of the lattice Boltzmann (LB) method to handle complex geometries. While the original LB method was initially constrained to uniform space-time lattices [1], a severe limitation for practical engineering purposes, nowadays several extensions have been developed which permit to do away with such a weakness. These include interpolation-supplemented finite-difference schemes [2,3], various types of finite-volume formulations [4,5], LB schemes with local grid refinement [6], as well as microscopic kinetic models in disordered lattices [7]. A particularly interesting option was recently proposed by Peng and co-workers [8–10], who imported powerful features of modern finite-volume techniques within the LB framework. This leads to a very significant upgrade of the finite-volume LB family, namely, the possibility of dealing with unstructured meshes, that is, nonuniform grids in which connectivity (the number of links emanating from each single node of the lattice) can change from node to node. These unstructured lattice Boltzmann schemes (ULBE for short) integrate the differential form of LBE using a *cell-vertex* finite-volume technique in which the unknown populations are placed at the nodes of the mesh and evolve based on the fluxes crossing the edges of the corresponding elements. Due to specific properties of the cell-vertex methodology, the resulting finite-volume LB schemes can operate on unstructured meshes, thereby providing a significant boost of geometrical flexibility which aligns LB with the most advanced computational fluid dynamics solvers. In this paper, we present further developments of the ULBE technique. In particular, we shall show that ULBE tolerates significant stretching without introducing any appreciable numerical viscosity effect to second order in the mesh size. This is very important for practical applications, since it permits a time-accurate description of transitional flows. A tentative theoretical explanation for this favorable behavior is also presented. Second, we introduce a set of boundary conditions which permit one to apply the ULBE technique to the case of flows with open boundaries. Finally, further directions of future research are also briefly surveyed.

I. UNSTRUCTURED FINITE-VOLUME FORMULATION OF LBE

Similar to all its predecessors, the unstructured finite-volume formulation first put forward by Peng *et al.* [8] begins with the single-time relaxation lattice Boltzmann equation in differential form:

$$\partial_t f_i + \vec{c}_i \cdot \vec{\partial}_x f_i = -(f_i - f_i^e)/\tau. \tag{1}$$

Here $f_i(\vec{x},t) \equiv f(\vec{x},\vec{v}=\vec{c}_i,t)$, $i=1,b$, is the probability of finding a particle at lattice site $\vec{x}$ at time t, moving along the lattice direction defined by the discrete speed $\vec{c}_i$. The left-hand side of this equation represents the molecular free-streaming, whereas the right-hand side represents molecular collisions via a single-time relaxation towards local equilibrium f_i^e on a typical time scale τ [11]. This local equilibrium is a (local) Maxwellian expanded to second order in the fluid speed:

$$f_i^e = \rho w_i [1 + \beta \vec{c}_i \cdot \vec{u} + \tfrac{1}{2}(\beta^2 \vec{c}_i \vec{c}_i - I) : \vec{u}\vec{u}], \tag{2}$$

where $\beta = 1/c_s^2$, c_s being the lattice sound speed, $1/\sqrt{3}$ in the present work, and I denotes the unit tensor. In the above, $\rho = \Sigma_i f_i$ is the fluid density and $\vec{u} = \Sigma_i \vec{c}_i f_i / \rho$ is the fluid speed. The relaxation time τ controls the fluid kinematic viscosity $\nu \simeq \tau$, the specific form of this relation depending on the details of the finite-volume scheme. In order to recover faithful fluid dynamics, the set of discrete speeds must be chosen such that mass, momentum, and energy conservation are fulfilled [17]. In the present work, we shall refer to the two-dimensional nine-speed model defined by the following discrete speeds [11]:

$$\vec{c}_i = \begin{cases} 0, & i=0 \\ \cos[(i-1)\pi/2], & i=1,4 \\ \sqrt{2}\cos[\pi/4 + (i-5)\pi/2], & i=5,8 \end{cases}$$

with weights $w_0 = 4/9$, $w_{1,4} = 1/9$, $w_{5,8} = 1/36$.

Following Peng *et al.* [8], we discretize the LBE in differential form (1) by introducing a tessellation based on triangular elements. To each node P of the discrete grid, we

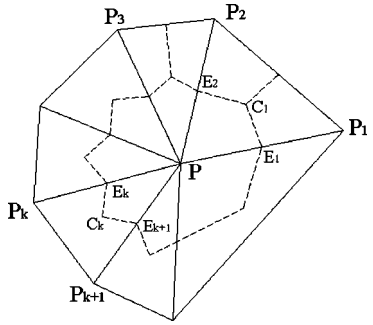

FIG. 1. Geometrical layout of the cell-vertex finite-volume discretization.

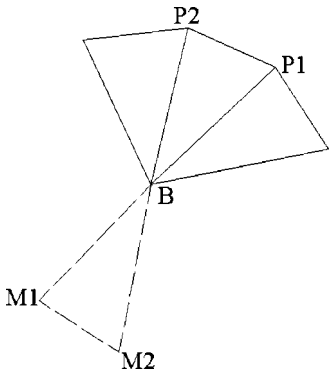

FIG. 2. Geometrical representation of the mirror method.

associate a set of $b=9$ discrete populations $f_i(P,t), i=1,b$ which represent the unknowns of the problem. The set of K triangles $T_k(P)$, $k=1,K$, which share P as a common vertex defines the finite element $T(P)$ associated with node P (see Fig. 1). Each of these K triangles is defined by the three vertices $T_k(P) \equiv [P,P_k,P_{k+1}]$, K being the connectivity of the unstructured mesh. To each triangle T_k is associated a finite volume $\Omega_k(P)$, defined by the union of the two subtriangles $\Omega_k^- = [P,E_k,C_k]$ and $\Omega_k^+ = [P,C_k,E_{k+1}]$, where C_k is the center of the triangle T_k and E_k, E_{k+1} are the midpoints of the edges PP_k, PP_{k+1}, respectively.

Application of the Gauss theorem to each finite volume $\Omega_k^{\mp}$, as combined with a first-order time marching, yields the following finite-difference equation:

$$f_i(P,t+dt) = f_i(P,t) + dt \sum_{k=1}^{K} (\Phi_{ik} - \Xi_{ik}), \tag{3}$$

where the sum k runs over the surface $\Sigma(P)$ obtained by joining the centers C_k with edges E_k: $\Sigma(P) = [E_1 C_1 E_2 \ldots E_K C_K E_{K+1}]$. In the above, V_P is the volume (area in 2D) of the control volume $\Omega_P = \cup_k \Omega_k$, and the cyclic condition $E_{K+1} = E_1$ ensures that the control volume Ω_P closes up. Finally, Φ_{ik}, Ξ_{ik} denote the streaming and collisional fluxes of the ith population coming from the kth volume Ω_k.

Note that fluxes over the internal edges PE_k, PC_k are not included because they cancel out identically (in-going flux from a neighbor volume is equal outgoing flux to that same volume). Evaluation of the fluxes in Eq. (3) requires the knowledge of the populations f_i at the edge and center locations. These values are obtained by interpolation within the given edge and triangles, respectively. More specifically,

$$f_i(E_k) = \frac{f_i(P) + f_i(P_k)}{2}, \tag{4}$$

$$f_i(C_k) = \frac{f_i(P) + f_i(P_k) + f_i(P_{k+1})}{3}. \tag{5}$$

Once these interpolation rules are defined, the calculation of the streaming fluxes is straightforward. The contribution of collisions arises from the integration of the collision term $(f_i - f_i^e)/\tau$ over each volume Ω_k:

$$\Xi_{ik} = V_P^{-1} \int_{\Omega_k} (f_i'/\tau) dV = V_P^{-1} \int_{\Omega_k^-} (f_i'/\tau) dV + V_P^{-1} \int_{\Omega_k^+} (f_i'/\tau) dV, \tag{6}$$

where $V^{\mp}$ are the volumes of $\Omega_k^{\mp}$ and $f_i' \equiv f_i - f_i^{eq}$. The resulting collisional flux is computed by calculating the local nonequilibrium distribution f_i' over $\Omega_k^{\mp}$ via a linear interpolation:

$$\Xi_{ik} = \frac{V_k^-/V_P}{3} [f_i'(P) + f_i'(E_k) + f_i'(C_k)] + \frac{V_k^+/V_P}{3} [f_i'(P) + f_i'(C_k) + f_i'(E_{k+1})]. \tag{7}$$

The resulting finite-volume equation takes the following general form:

$$f_i(P,t+dt) = f_i(P,t) + dt \sum_{k=0}^{K} S_{ik} f_i(P_k,t) - \frac{dt}{\tau} \sum_{k=0}^{K} C_{ik} [f_i(P_k,t) - f_i^e(P_k,t)], \tag{8}$$

where index $k=0$ denotes the pivotal point P. The detailed expressions of the streaming and collision matrices S_{ik} and $C_{ik} = C_k \delta_{ik}$ are obtained by direct application of the interpolation rules (4) and (7). The result is

$$S_{i0} = 0, \quad S_{ik} = \vec{c}_i \cdot \vec{N}_k / V_P, \quad k = 1,K \tag{9}$$

and

$$C_0 = 1/3, \quad C_k = \frac{V_{k-1} + V_k}{3 V_P}, \quad k = 1,K. \tag{10}$$

In the above, we have defined

$$\vec{N}_k = [\tfrac{5}{12}(\vec{A}_{k-1}^+ + \vec{A}_k^-) + \tfrac{2}{12}(\vec{A}_{k-1}^- + \vec{A}_k^+)], \quad k = 1,K,$$

where $\vec{A}_k^{\mp}$ are the vectors normal to the surfaces (lines in 2D) $E_k C_k$, $C_k E_{k+1}$, with magnitude equal to the size (length in

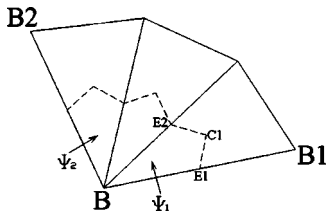

FIG. 3. Geometrical layout for boundary elements. The fluxes Ψ_1, Ψ_2 across the boundary edges BB_1 and BB_2 need to be explicitly computed.

2D) of these surfaces. Similarly, $\vec{A}_{k-1}^{\mp}$ associate with surfaces $E_{k-1}C_{k-1}$ and $C_{k-1}E_k$, respectively.

It is readily checked that the following sum rules hold:

$$\sum_{k=0}^{K} S_{ik}=0, \quad \sum_{k=0}^{K} C_{ik}=1 \quad \forall i.$$

These sum rules play an important role in the theoretical analysis of the scheme, as detailed in the sequel.

II. BOUNDARY CONDITIONS

The above procedure applies to both internal and boundary nodes. However, in the case of boundary nodes, the corresponding control volumes do not close up, leaving two external edges exposed on the boundary (see Fig. 3). Several strategies can be chosen to deal with these boundary edge fluxes, but three methods have been used so far: (i) equilibrium method, (ii) mirror method, (iii) covolume method.

The equilibrium method consists in setting the edge values of the populations to the corresponding equilibrium values, based on the specified values of the density and velocity field at the boundary. This method is very simple, but of limited use, since it cannot handle situations with significant gradients at the boundary (a commonplace in most applications).

The mirror method consists in introducing ghost nodes at the boundary, which are defined as the mirror images of the corresponding internal nodes, pivoted around the boundary node B (see Fig. 2). Prior to evaluation of the streaming fluxes, the mirror populations are fixed by a simple second-order interpolation:

$$f(M_k)=2f(B)-f(P_k).$$

Once this is done, the boundary node B can be updated as if it were an ordinary internal node. This procedure is very transparent and can deal with boundary gradients. However, it may lead to topological ambiguities for generic boundaries, because the volume element associated with a boundary node does not close up if the boundary is curved.

Finally, in the covolume method, the edge fluxes are evaluated explicitly by using interpolation at the boundary edges (see Fig. 3):

$$f(E_k)=\frac{f(B)+f(B_k)}{2}.$$

This is slightly more complicated to program than the previous two, because it requires to account explicitly for edge fluxes which are not seen by internal nodes. However, the covolume method supports boundary gradients and it works for the generic boundary geometries.

The above prescriptions cover an important class of boundary conditions, but are not clear as how to handle open boundaries—a case of great importance for practical applications.

Indeed, our experiments indicate that none of the three boundary procedures described above is able of handling open flows in a satisfactory way (to the best of our knowledge, no open-flow application of the ULBE method has been presented to date). To cope with this problem, we have developed the following procedure.

A. Inlet-outlet boundary conditions

At both inlet and outlet sections, the computational domain is augmented with one (or more) buffers of regular, straight triangles. The scope of these regular layers is to ensure that the last-but-one row of nodes faces a corresponding neighbor along the x direction, so that, by imposing the same velocity field on these two rows of nodes, a zero-longitudinal-gradient boundary condition automatically results. This very simple recipe is found to yield acceptable results where none of the three boundary conditions described above would work, as it will be documented shortly.

Before doing so, a few theoretical considerations are in order.

B. Theoretical considerations

To date, the ULBE scheme has been successfully demonstrated for a number of simple test benchmarks, such as Couette flow, driven cavity flow, and others [8–10,12]. Among others, these tests indicated that ULBE exhibits a fairly low amount of numerical diffusion, a somehow intriguing property for an unstructured finite-volume method. However, no theoretical analysis of this property has been presented to date. Here we outline the basic points of this analysis, leaving full details to a separate publication.

The distinctive mark of *all* finite-volume formulations of LBE is a clear-cut separation between the set of discrete speeds $\vec{c}_i, i=1,b$ and the spatial grid, most specifically the set of nearest-neighbor connectors:

$$\vec{d}_k \equiv P_k - P, \quad k=0,K.$$

In the limit where these two sets coincide,

$$\vec{c}_i dt = \vec{d}_i, \quad b=K \tag{11}$$

we would expect ULBE to reproduce the standard LBE, a property called *consistency* in early finite-volume formula-

tions [4,13]. Consistency is a comfortable property because it ensures that the finite-volume LBE inherits all the familiar (and nice) properties of standard LBE in the limit of a uniform lattice. In particular, the fact that numerical diffusion amounts to a constant value $-1/2$ everywhere, permits to reabsorb it exactly within the definition of the effective lattice fluid viscosity $\nu=c_s^2(\tau-1/2)$.

It is readily shown that this property does *not* hold for the present ULBE.

To see this, it is sufficient to inspect the specific form of the streaming coefficients S_{ik}, Eq. (9). The quantity $S_{ik}dt/V_P$ represents the fractional volume swept by the ith population along the perpendicular to the surface Σ_k in a time lapse dt. Consequently, it is the analog of the Courant-Friedrichs-Lewy number controlling the numerical stability of the scheme $(S_{ik}dt/V<1)$.

In order to recover the standard LBE in the limit $\vec{c}_i dt = \vec{d}_k$, we require $S_{i0}dt=-1$, $S_{i,k}dt=\delta_{ik}$. It is readily seen that this is not the case. Lack of consistency with standard LBE is not necessarily a flaw of ULBE: it simply warns us that some of the familiar properties of the standard LBE are not inherited by ULBE.

A complete theoretical analysis of the numerical properties of ULBE requires a full-fledged Chapman-Enskog procedure, which is left for a future publication. Much insight can, however, be gained by a simpler approach based on the inspection of the dispersion relation associated with the ULBE scheme. For the purpose of highlighting the role of grid discreteness on the linear properties of the ULBE scheme, it is sufficient to concentrate on the collision-free version of the differential LBE (1). By representing the density distribution function $f_i(\vec{x},t)$ in Fourier series as $f_i(\vec{x},t) \sim e^{i(\vec{p}\cdot\vec{x}-\omega t)}$, where ω is the (complex) frequency and $\vec{p}$ the wave vector, and Fourier transforming the collision-free ULBE, we obtain

$$e^{-i\omega dt}=1+dt\sum_{k=0}^{K} S_{ik}e^{-i\vec{p}\cdot\vec{d}_k}. \tag{12}$$

In the continuum, these two quantities are related by the free-wave dispersion relation,

$$\omega_R=\vec{p}\cdot\vec{c}, \quad \omega_I=0,$$

where subscripts R,I denote the real and imaginary parts, respectively. As is well known, the second-order terms of the form C_2p^2 in the expression of ω_I associate with numerical *diffusion*, whereas the third-order terms in ω_R correspond to numerical *dispersion*.

A remarkable property of the standard LBE scheme is that the continuum dispersion relation is *exactly* reproduced on the discrete light cones $d\vec{x}_i=\vec{c}_i dt$, simply because the particles propagate along the directions of the discrete grid. More precisely, the viscosity of the plain LBE scheme consists of two separate contributions:

$$\nu=c_s^2(\tau+\tau_P). \tag{13}$$

In the above, τ is the physical contribution due to collisional relaxation, whereas τ_P is a purely numerical contribution due to the second-order expansion of the streaming operator. For standard LBE, $\tau_P=-1/2$, corresponding to a negative diffusion. The remarkable point is that this numerical diffusion can be incorporated within the effective viscosity of the LBE fluid according to expression (13). On the other hand, since $d\vec{x}_i=\vec{c}_i dt$, the scheme is also dispersion-free at all orders. Such useful properties are generally lost in a finite-volume formulation with arbitrary geometry, where a certain degree of numerical diffusion and dispersion must be anticipated.

To appreciate this point quantitatively, one has to solve the dispersion relation (12). A few general remarks can be made without actually solving this equation in detail. By summing the squares of the real and imaginary parts of Eq. (12), and taking the ratio of the imaginary to the real part, we obtain the following relations:

$$e^{2\omega_I dt}=1+2C_i dt+(S_i^2+C_i^2)dt^2, \tag{14}$$

$$tg(\omega_R dt)=\frac{S_i dt}{1+C_i dt}, \tag{15}$$

where we have set

$$C_i\equiv\sum_k S_{ik}\cos\phi_k, \quad S_i\equiv\sum_k S_{ik}\sin\phi_k, \quad \phi_k\equiv\vec{p}\cdot\vec{d}_k.$$

In order to appreciate the effects of space-time discreteness at various orders, the above relation is best expanded in the Taylor series of both dt and ϕ_k.

At zeroth order in dt, we obtain $\omega_I=0$, and no information on ω_R.

At the first order (the one relevant to linear advection), we obtain

$$\omega_I=C_i, \quad \omega_R=S_i.$$

By expanding C_i and S_i to first order in space, the former gives again $\omega_I=0$ (owing to the sum rule $\Sigma_{k=0}^K S_{ik}=0$), whereas the latter yields

$$\omega_R=\sum_k S_{ik}\vec{d}_k\cdot\vec{p},$$

which identifies the propagation speed of collective motion as

$$\vec{V}_i=\sum_k S_{ik}\vec{d}_k.$$

Based on the expression of S_{ik}, Eqs. (9), it is seen that this reduces to the standard LBE value $\vec{c}_i$, only if the tensor

TABLE I. Percentage error versus grid distortion between present numerical results and the analytic solution.

δ	ϵ
0.00	0.017
0.15	1.26
0.3	1.53
0.4	4.34

$\Sigma_k \vec{d}_k \vec{N}_k$ becomes (proportional to) the identity. In general, this is not the case, the propagation speed depends on the local position and contains higher-order contributions in the wave vector $\vec{p}$ (numerical dispersion effects).

Proceeding to next order in space, we get a new contribution to the imaginary part, corresponding to (numerical) diffusion,

$$\omega_I = \sum_k \frac{1}{2} S_{ik} \vec{d}_k \vec{d}_k : \vec{p}\vec{p}.$$

This identifies a (purely numerical) diffusion tensor as

$$\vec{\vec{D}}_i \equiv \frac{1}{2} \sum_k S_{ik} \vec{d}_k \vec{d}_k ,$$

which is the analog of the $\vec{c}_i \vec{c}_i/2$ term in the standard LBE.

On a general grid, this diffusion tensor cannot be strictly homogeneous, nor can it be isotropic. Interestingly enough, however, it can be close to zero. Consider in fact the distinguished limit in which each subvolume Ω_k has a mirror partner Ω_{k*} such that $\vec{N}_k + \vec{N}_{k*} = 0$. If this mirror symmetry holds, the above sum in k annihilates the diffusion tensor by mere symmetry. It is interesting to point out that the ULBE scheme does indeed have mirror symmetry in the limit of a regular, uniform mesh with $b = K$. As a result, if mirror symmetry is only mildly broken, then numerical diffusion can be correspondingly small. In addition, further cancellations are expected on a scale larger than the typical size of the elements, due to spatial averaging over an ensemble of ''random'' elements.

This provides a theoretical clue on the reasons why numerical simulations with ULBE show a very low degree of numerical diffusivity. One may wonder whether the collision operator is going to change this picture. A similar analysis on the collision matrix C_{ik} shows that this is not the case. Owing to the sum rule $\Sigma_k C_k = 1$, discretization effects on the collision operator do alter the bare value $\omega_I = 1/\tau$, but only at second order in p (hyperviscous effects).

III. NUMERICAL RESULTS

In the present section we provide a numerical demonstration of the ideas discussed above.

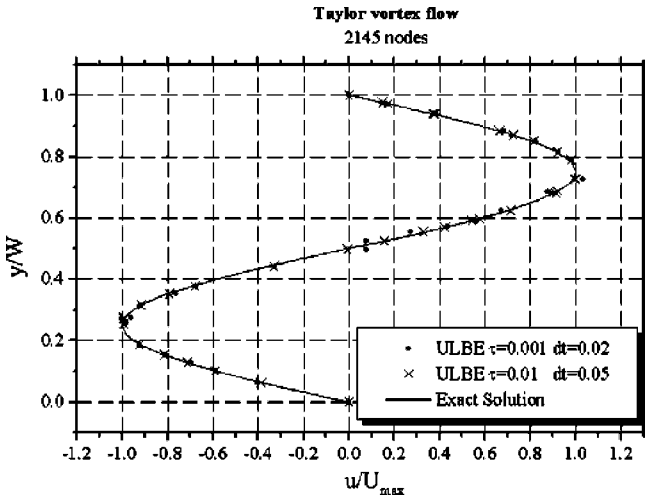

FIG. 4. Streamwise velocity profile for the Taylor-vortex simulation.

A. Numerical viscosimeter

As a preliminary step, we show that numerical viscosity effects are very small, within second-order accuracy in space. In order to measure the numerical viscosity, we consider a two-dimensional Taylor-vortex configuration in a box of size W and let it freely decay in time. The numerical results are confronted with the analytical solution:

$$u = -u_{max} \cos(p_1 x) \sin(p_2 y) e^{-\nu(p_1^2 + p_2^2)t},$$

$$v = v_{max} \sin(p_1 x) \cos(p_2 y) e^{-\nu(p_1^2 + p_2^2)t}.$$

In Fig. 4 we show the profile u/u_{max} versus y/W, as obtained by ULBE with $p_1 = 0$, $p_2 = 2\pi/W$, and compared with the analytical solution. The grid contains 2145 nodes, and therefore second-order effects of numerical viscosity are expected to be of the order of $1/2145 - 5 \times 10^{-4}$. To explore this regime, we have changed the relaxation parameter τ through the following sequence: $\tau = 0.01$, 0.0025, 0.001, and $dt = 20\tau$. On the scale of the picture, all the results appear to be within a few percent of the analytic solution, as computed with a theoretical viscosity:

$$\nu = c_s^2 \tau. \tag{16}$$

Residual viscosity does not appear to contaminate this relation even with τ as low as 0.001, which is a clear indication of second-order accuracy (a numerical viscosity $\nu_n \sim 1/2000$ would yield a 30% error). This confirms previous

TABLE II. Percentage error versus number of elements of a regular grid between the numerical results and the analytic solution.

Elements	ϵ
1024	0.071
4096	0.017
6400	0.011

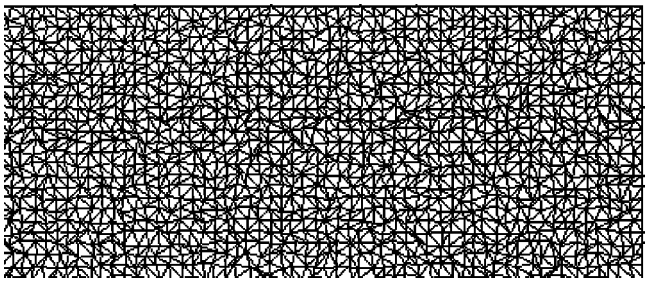

FIG. 5. Grid for the forced Poiseuille flow with periodic boundary conditions.

claims [9] and extends them to a second-order regime (previous work used $\tau > 0.01$, too high to be conclusive on second-order effects).

To gain a better understanding of this matter, a new series of simulations of the vortex Taylor with increasing degree of distortion has been performed and the relative error as compared to the exact solution is provided for each distorted grid (see Table I): Starting from a structured layout of nodes $\vec{x}_n$, $n=1,N$, a distorted configuration is generated by changing the node locations by random displacements $\vec{r}_n$, $\vec{x}'_n = \vec{x}_n + \vec{r}_n$. Distorted configurations are classified according to their "distance" from the structured one, defined as $\delta = \max_m\{|l'_m/l_m - 1|\}$, where l_m and l'_m denote the lengths of the links of the regular and distorted configurations, respectively. The error relative to the exact solution, defined as $\epsilon = \Sigma_n|(u_n - u_n^{exact})/u_{max}|$, as a function of δ is reported in Table I.

This table shows that the numerical error (not entirely due to diffusion but also due to higher-order effects, such as dispersion) remains within a few percent up to fairly substantial degree of grid distorsions. In addition, we have also measured the error scaling with the number of elements, as shown in Table II.

These data confirm that the error decreases linearly with the number of elements, hence quadratically with the linear size of the mesh cell.

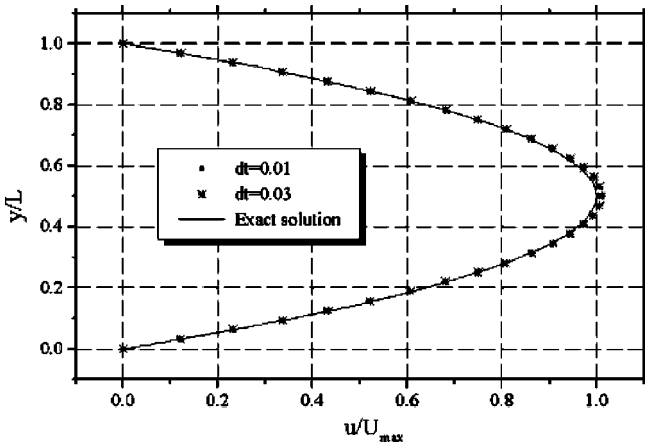

FIG. 6. Parabolic profile for forced Poiseuille flow with periodic boundary conditions.

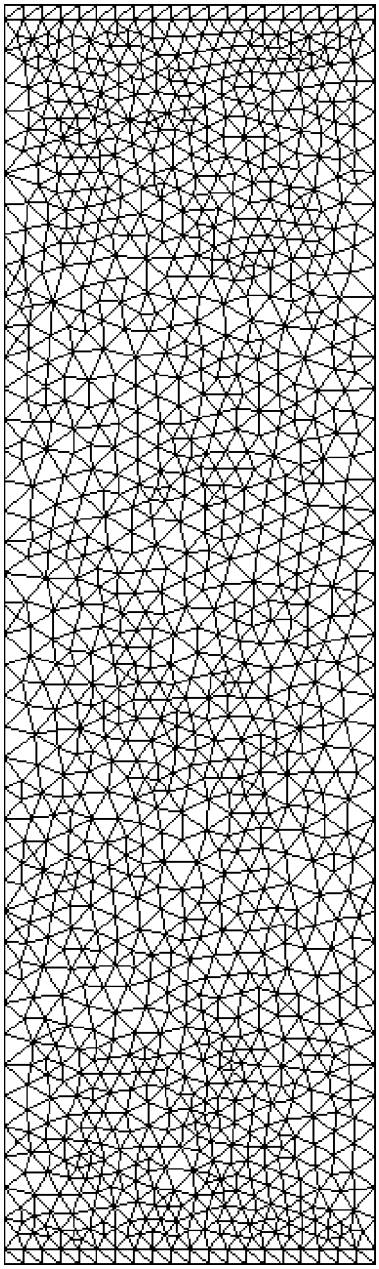

FIG. 7. Computational grid for the impulsively started Poiseuille flow with open outlet.

B. Driven channel flow

As a first test case for open flows, we consider a two-dimensional channel flow driven by a constant volumetric force. Boundary conditions are no-slip at top and bottom walls and periodic at inlet (or outlet). The flow is forced to a maximum speed $U_M = 0.4$, while the other parameters are $\tau = 0.1$, $dt = 0.01$–0.03. The grid contains 2360 elements, covering a domain of length $L = 96$ and width $W = 32$ (see Fig. 5) corresponding to a Reynolds number $\mathrm{Re} = 1000$.

The steady-state longitudinal velocity profile is shown in Fig. 6, from which quite good agreement with analytical results is apparent. For this test case, both mirror and covolume boundary conditions were found to yield results in good agreement with the analytical solution. However, flow peri-

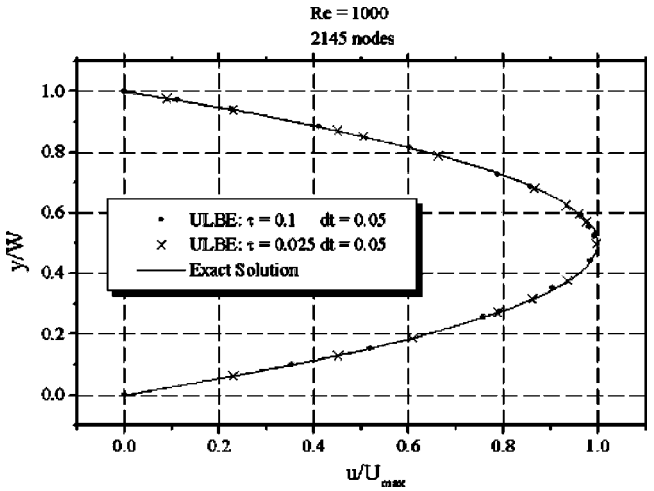

FIG. 8. Parabolic profile for the impulsively started Poiseuille flow with open outlet.

odicity at inlet and outlet rules out a number of practical applications, and more realistic boundary conditions need to be addressed, as detailed in the following.

C. Impulsively started channel flow

Next we focus the important case of flows with open outlets. The flow is initially at rest (zero speed) and is impulsively started by forcing a parabolic profile with maximum speed U_M at the inlet section. At the upper and lower walls, no-slip boundary conditions (zero-speed) boundary conditions are imposed with the standard covolume method. At the outlet, the condition of zero-longitudinal gradients is imposed via the covolume method with regular outlet buffers, as discussed in Sec. II A (see Fig. 7). The numerical parameters are $W=32$, $L=96$, $U_M=0.08$, $\tau=0.025-0.1$, corresponding to the Reynolds number $\mathrm{Re}=U_M H/\nu=72$. The computational domain is covered with 2360 elements and 1241 nodes. The simulation runs over 300 000 time steps of length $dt=0.05$, spanning a time lapse of 9000 time units, corresponding to almost nine recirculation times. The steady parabolic profile is shown in Fig. 8, from which a very nice agreement with the analytical solution is observed.

The use of regular buffers at the inlet and outlet was found to be instrumental to achieve these results. It should also be mentioned that a few adjustments of the grid were required before the correct result could be obtained. These adjustments amount to choosing the right thickness and number of elements in the inlet and outlet buffer regions. Further work is surely needed to make the open-boundary conditions more robust and grid insensitive.

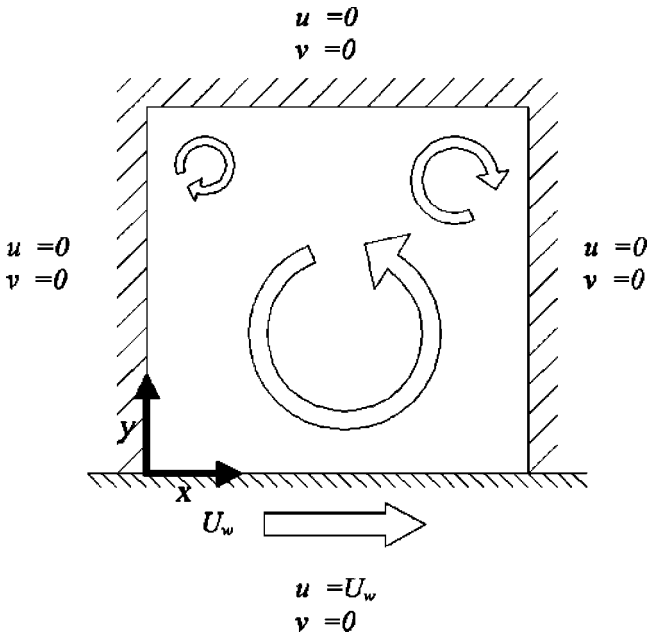

FIG. 9. Sketch of the geometry for the driven-cavity flow simulation.

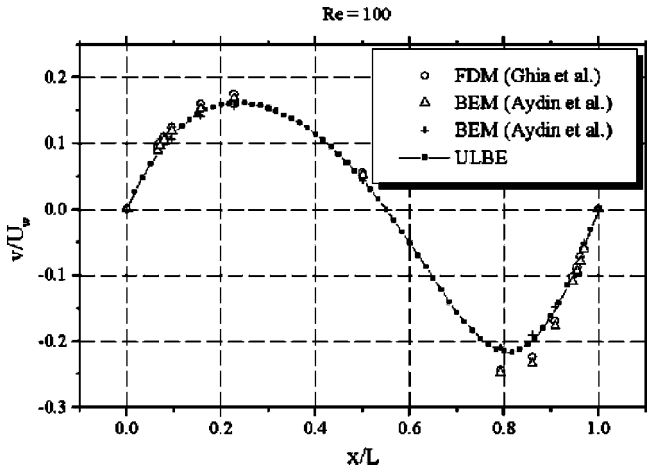

FIG. 10. Centerline longitudinal velocity profile for the cavity flow at Reynolds number 100.

D. Cavity flow

Finally, we present a test in which the nonlinear component of the Navier-Stokes plays a major role. This is the standard lid-driven cavity flow (see Fig. 9). Boundary con-

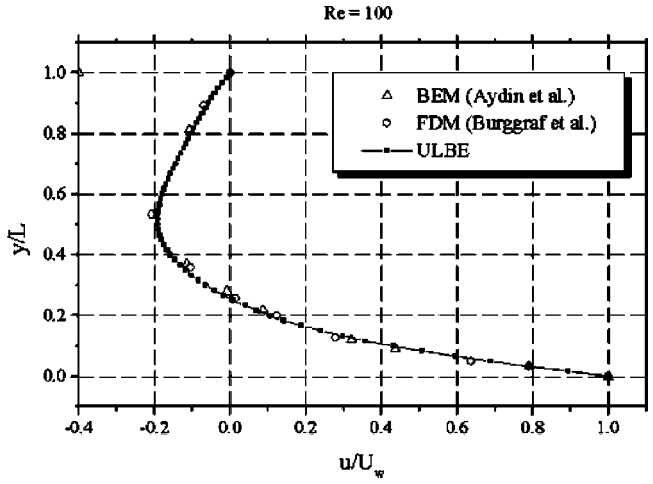

FIG. 11. Centerline transversal velocity profile for the cavity flow at Reynolds number 100.

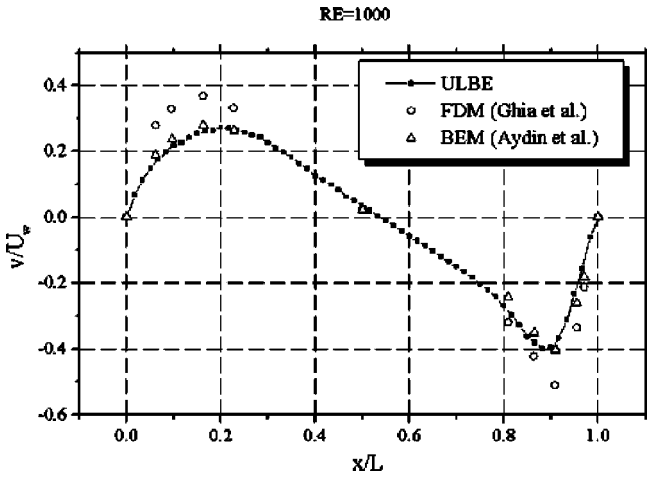

FIG. 12. Centerline longitudinal velocity profile for the cavity flow at Reynolds number 1000.

ditions are as follows: at fixed walls we use the covolume method with zero speed in the local equilibria. Moving walls are handled the same way, but with a prescribed nonzero speed U_W in the local equilibria. As usual, an ambiguity arises at the corner points, which belong to both fixed and sliding walls. In the standard LBE, either choice is applicable and would yield reasonable results because three out of four diagonal speeds do not propagate inside the computational domain. Of course, accuracy depends a great deal on the details of the corner boundary condition and affects the maximum value of the Reynolds number which can be reliably simulated. In finite-volume implementations the situation is more delicate, because all populations contribute to the incoming fluxes from the boundaries [10]. Recipes to deal with corners are given and numerically demonstrated at Re$=100$, 400, 1000 in Ref. [12]. The results show a deterioration with the Reynolds number, as witnessed by the small-scale wiggles well apparent in the velocity profiles at Re $=1000$. More robust strategies to deal with corners are clearly needed.

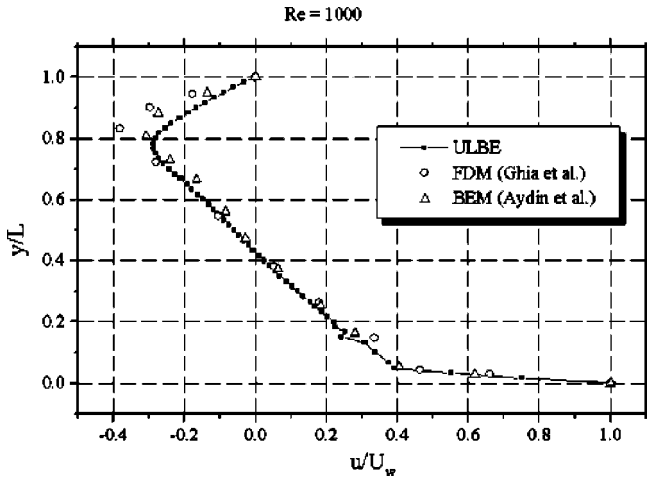

FIG. 13. Centerline transversal velocity profiles for the cavity flow at Reynolds number 1000.

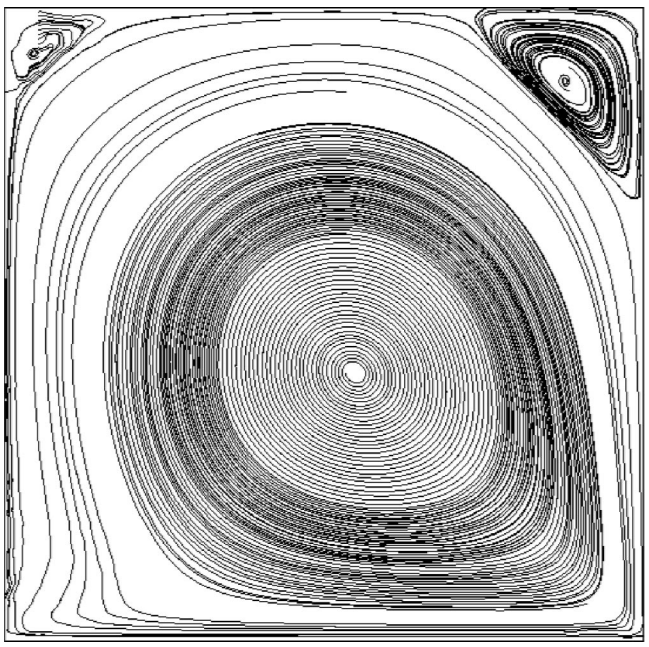

FIG. 14. Flow streamlines for the cavity flow at Reynolds number 1000.

We have repeated the same simulations at Re $=100$, 400, 1000, with the numerical parameters $\tau=0.1$, $dt=0.01$, and 3598 nodes, and using the covolume boundary condition. We found that the best results are obtained by excluding the corners, namely, removing a single triangle at each of the four corners.

Although this provisional solution might result in local distortions of the secondary vortices at Re>1000, it shows nonetheless encouraging results. In particular, owing to the flexibility of the unstructured grid, one can arguably minimize the aforementioned distortions by reducing the size of the corner element to be removed.

The transverse profiles of the longitudinal and transverse velocities $u(y)$, $v(y)$ at the centerline $x=L/2$, are shown in Figs. 10 and 11 for the case Re$=100$. From these figures nice agreement with previous literature data, including finite-differences [14] and boundary-element methods [15], is observed. A similar statement applies to the case Re$=400$, not shown here. Finally, the longitudinal and transversal velocity profiles for the case Re$=1000$ are shown in Figs. 12 and 13. These pictures show no sign of numerical wiggles, witnessing an interesting improvement over previous literature data. We also display the steady flow field configuration (Fig. 14),

TABLE III. Cartesian coordinates of the three main vortices at Re$=1000$. ULBE, present method; Ref. [14], finite-difference method; Ref. [15], boundary element method; Ref. [16], standard LBE.

Vortex position	ULBE	Refs. [14–16]
Primary $x/L,y/L$	0.565,0.386	0.555–0.5557,0.389–0.395
Left $x/L,y/L$	0.051,0.959	0.051–0.953
Right $x/L,y/L$	0.893,0.883	0.891–0.875

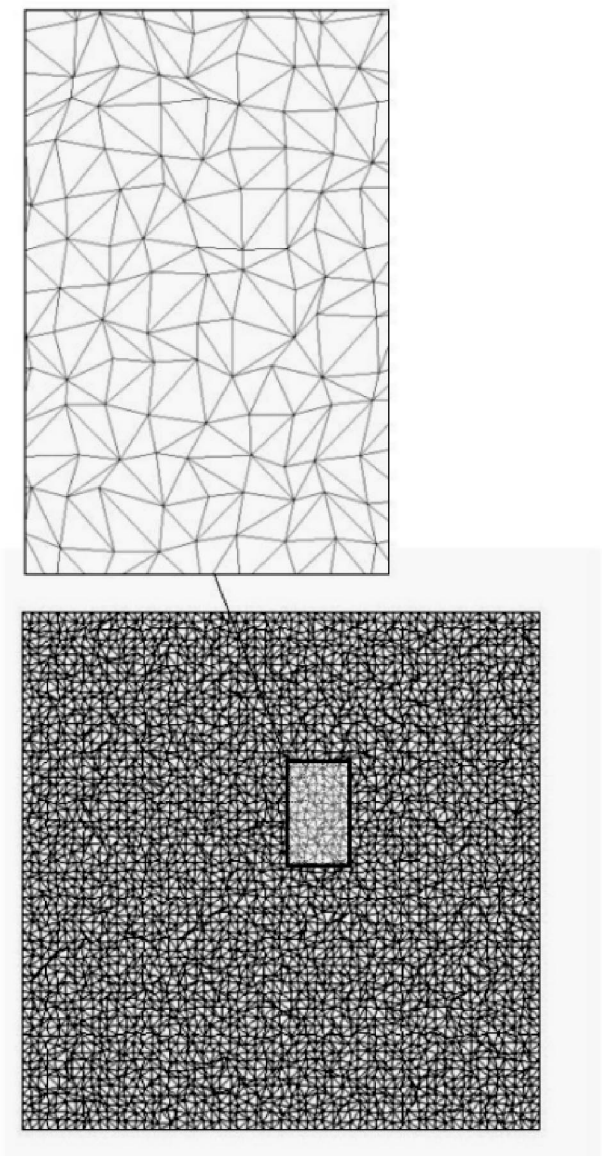

FIG. 15. Unstructured grid for the cavity-flow calculation. The inset shows a close-on of the grid, which reveals a significant distortion of the geometrical elements.

from which the existence of a primary and two secondary vortices is clearly observed. Quantitative data regarding the position of these vortices are provided in Table III. Good agreement with previous methods, including finite-differences [14], boundary elements [15], and standard BGK [16] is observed.

Before concluding, we wish to emphasize that the present results have been obtained by using unstructured grids with a substantial degree of local distortion, as evidenced by the inset of Fig. 15.

SUMMARY AND FUTURE DIRECTIONS

This work presents a series of results. First, it provides further numerical evidence that the unstructured finite-volume LBE proposed by Peng *et al.* introduces fairly small numerical viscosity, actually compatible with second-order accuracy. A semiquantitative theoretical explanation for this nice behavior is also proposed. Second, we have shown that the above conclusion seems to hold also in the presence of a substantial stretching of the grid. Third, a boundary condition, which extends the viability of ULBE to an important class of open flows, has been presented and numerically demonstrated. Finally, we have shown that cavity flow simulations can be taken to relatively high-Reynolds numbers with no sign of numerical instabilities, by simply rounding off the corners of the computational domain.

Despite these encouraging results, much remains to be done to put ULBE on a firm basis for complex physics and engineering applications.

First, more systematic and robust procedures to deal with a wider class of boundary conditions need to be developed. These include flows with open boundaries, as well as corners between rigid and sliding walls. A full-fledged theoretical analysis of the numerical properties of ULBE makes also an important subject for future research. Furthermore, the computational efficiency of ULBE versus standard LBE as well as state-of-the-art finite-volume techniques needs to be assessed. It is clear that ULBE is computationally more expensive than the traditional LBE (on a single-node basis) because both streaming and collision operators are nonlocal. On the other hand, it is clear that ULBE is not meant to be a replacement of the standard LBE, but represents an additional option which is increasingly valuable with rising geometrical complexity. However, the elegance of the method, combined with its outstanding geometrical flexibility, holds promise to significantly advance lattice Boltzmann research in the years to come.

ACKNOWLEDGMENTS

Financial support from the NATO Collaborative Link Grant No. PST.CLG.976357 and CNR Grant No. CNRC00BCBF-001 is kindly acknowledged.

[1] R. Benzi, S. Succi, and M. Vergassola, Phys. Rep. **222**, 145 (1992); D. Wolfe-Gladrow, *Lattice Gas and Lattice Boltzmann Methods* (Springer-Verlag, Berlin, 2000); S. Succi, *The Lattice Boltzmann Equation for Fluid Dynamics and Beyond* (Oxford University Press, Oxford, 2001).

[2] X. He, X. Shan, and G. Doolen, Phys. Rev. E **57**, R13 (1998).

[3] N. Cao, S. Chen, S. Jin, and D. Martinez, Phys. Rev. E **55**, R21 (1997); X. He, L. Luo, and M. Dembo, J. Comput. Phys. **129**, 357 (1996).

[4] F. Nannelli and S. Succi, J. Stat. Phys. **68**, 401 (1992); S. Succi, G. Amati, and R. Benzi, *ibid.* **81**, 5 (1995).

[5] H. Chen, Phys. Rev. E **58**, 3955 (1998); H. Chen, C. Teixeira, and K. Molvig, Int. J. Mod. Phys. C **9**, 1281 (1998).

[6] O. Filippova and D. Haenel, J. Comput. Phys. **147**, 219 (1998).

[7] I.V. Karlin, S. Succi, and S. Orszag, Phys. Rev. Lett. **82**, 5245 (1999).
[8] G. Peng, H. Xi, and C. Duncan, Phys. Rev. E **58**, R4124 (1998).
[9] H. Xi, G. Peng, and S-H. Chou, Phys. Rev. E **60**, 3380 (1999).
[10] H. Xi, G. Peng, and S-H. Chou, Phys. Rev. E **59**, 4675 (1999); G. Peng, H. Xi, and S-H. Chou, Int. J. Mod. Phys. C **10**, 1003 (1999).
[11] Y. Qian, D. d'Humières, and P. Lallemand, Europhys. Lett. **17**, 479 (1992).
[12] Y.T. Chou, C. Shu, and Y. Peng, J. Stat. Phys. **107**, 539 (2002).
[13] G. Amati, S. Succi, and R. Benzi, Fluid Dyn. Res. **19**, 289 (1997).
[14] K.N. Ghia, C.T. Ghia, and C. Shin, J. Comput. Phys. **48**, 387 (1982); R. Schreiber and H. Keller, *ibid.* **49**, 310 (1983).
[15] M. Aydin and R.T. Fenner, Int. J. Numer. Methods Fluids **37**, 45 (2001).
[16] R. Mei, L. Luo, and W. Shyy, J. Comput. Phys. **155**, 307 (1999).
[17] F. Higuera, S. Succi, and R. Benzi, Europhys. Lett. **9**, 345 (1989).